Multi-hop Relaying Distribution Strategies for Terahertz-band Communication Networks: A Cross-layer Analysis

Qing Xia, *Member, IEEE*, and Josep M. Jornet, *Senior Member, IEEE*

***Abstract*—Terahertz (THz) band (0.1-10 THz) communication is envisioned as a key wireless technology to satisfy the need for wireless Terabit-per-second (Tbps) links in 6G systems. The THz band supports very large channel bandwidths with the cost of very high propagation losses. On the one hand, the absorption by water vapor molecules manifests itself in the form of absorption lines that broaden in frequency with distance, resulting into a highly distance-dependent channel bandwidth. On the other hand, the very high spreading or free-space losses require the use of highly directional antennas (DAs) simultaneously in transmission and reception at all times. As with the bandwidth, the beamwidth of such DAs is also related with the transmission distance, and introduces severe synchronization and, correspondingly, delay challenges. These issues become even worse when the system needs to support up to Tbps peak data-rates. The end-to-end (E2E) delay and, correspondingly, effective throughput in multi-hop THz communication networks can drastically suffer if all these peculiarities are not taken into account. In this paper, multi-hop relaying distribution strategies are developed for THz-band communication to minimize the multi-hop E2E delay by considering cross-layer effects between the THz channel, highly DAs, nodes' buffer and the physical, link and network layers.**

***Index Terms*—Terahertz communication, Multi-hop relaying, Cross-layer analysis, Ultrabroadband networking**

I. INTRODUCTION

The way in which we create, share (upload) and consume (download) information has drastically changed in the last decade. Not only we have more wirelessly connected devices (e.g., 8.8 billion mobile devices connected to the Internet in 2018 [1]), but their connections support higher data-rates (e.g., download peaks of 20 Gigabits-per-second or Gbps in 5G New Radio or NR). Early discussions on 6G systems point to 1 Terabit-per-second (Tbps) of downlink peak data rate as a reasonable target rates for the next generation of wireless networks, both on the academic [2] as well as on the industry [3] sides. This is a 50 times increase over 5G NR. Achieving this goal will require the adoption of bandwidths larger than the 800 MHz with channel aggregation in 5G NR Frequency Range 2 (FR2) in the millimeter-wave band. For example, even when utilizing 8 parallel MIMO channels with 1,024 QAM per channel, more than 10 GHz of bandwidth would be needed to reach 1 Tbps.

In this context, terahertz (THz)-band (0.1 THz to 10 THz) communication is envisioned as a key technology for 6G [4]–[7]. The THz-band communications enable many exciting applications both in traditional or macroscale scenarios, such as fully immersive high-definition virtual reality and ultra-high-capacity wireless backhauling, as well as in innovative nanoscale scenarios, including wireless networks on chip, wireless nanosensor networks and the Internet of Nano-Things. For many decades, the lack of compact high-power signal sources and high-sensitivity detectors able to work at room temperature hampered the use of the THz band for any application beyond sensing. However, many recent advancements with several device technologies [8] are finally closing the so-called THz gap. Utilizing such technologies, experimental testbeds for communications across multiple frequencies in the THz band and for communication distances ranging from few centimeters to hundreds of meters and more have been built [9].

The THz band provides wireless communication devices with an unprecedentedly large channel bandwidth, at the cost of a similarly very high propagation loss [10]–[13]. More specifically, first, due to the shorter wavelength of THz-band signals, resonant THz antennas are smaller and, thus, able to intercept a smaller fraction of the power radiated by the transmitter. Second, molecular absorption selectively attenuates THz-band radiation. In particular, THz radiation can induce internal vibrational modes in different types of molecules, effectively converting electromagnetic energy into kinetic energy. The main absorber of THz radiation is water vapor, which effectively divides the THz band in a collection of discrete absorption-free transmission windows, each tens to hundreds of GHz wide. While the absorption frequencies or lines are fixed, their strength and width depends on the medium temperature and pressure, as well as on the density and spatial distribution of the absorbing molecules. For a homogeneous spatial distribution of molecules, increasing the communication distance also means increasing the number of molecules that the signal interacts with. Such increase leads to both higher attenuation but also broadening of the absorption lines. As a result, the available bandwidth, i.e., the spacing between absorption lines, is reduced with distance. Such behavior introduces several challenges and opportunities at the physical layer, including for example the design of adaptive bandwidth modulations [14], [15]. In addition, THz-

---

Q. Xia completed this work when she was a Ph.D. student in the Department of Electrical Engineering at the University at Buffalo, the State University of New York.

J. M. Jornet is with the Department of Electrical and Computer Engineering, Northeastern University, Boston, MA, USA.

This work was supported in part by the US Air Force Research Laboratory Grant FA8750-20-1-0200 and the US National Science Foundation Grant CNS-2011411.

band signals can interact with obstacles in different ways, including full and partial reflection, absorption and transmission. Generally, THz signals do not propagate through walls, windows and humans, but are partially absorbed and partially reflected.

To compensate for the very high propagation losses and given the very limited power of THz transceivers (up to a few hundreds of mW at sub-THz frequencies when utilizing new semiconductor materials and advanced manufacturing techniques, but much less when relying on CMOS technologies [16]), highly directional antennas (DAs) are needed simultaneously in transmission and reception to establish communication links beyond a few meters [17], [18]. However, the utilization of the highly DAs introduces many challenges as we move up in the protocol stack design. For instance, tighter spatial synchronization between transmitter and receiver is required to solve the crucial deafness problem caused by antenna misalignment [17], [19] in the link layer medium access control (MAC). Also, new neighbor discovery protocols are needed to adapt to the highly directional THz communication networks [20], since the majority of existing solutions assume that communication can be established with at least one omnidirectional/quasi-omnidirectional antenna at transmission side or reception side [21], [22], which, unfortunately, is insufficient to overcome the much higher propagation loss in THz-band communication networks.

Beyond continuously increasing the antenna gains, other strategies to meaningfully increase the communication distance [23] include the development of multi-hop relaying strategies. While this is a very well-explored topic at lower frequencies [24]–[26], existing solutions cannot be simply reused, because they do not capture the peculiarities of the aforementioned THz channel and THz devices and their impact on the link layer. More specifically, due to the unique distance-dependent behavior of the available bandwidth, the reduction of the transmission distance results in twofold benefits. On the one hand, as in any other wireless communication system, by reducing the transmission distance between nodes and maintaining the transmission power, the signal-to-noise ratio (SNR) increases and higher order modulations can be utilized to increase the data-rates. On the other hand, because of the behavior of molecular absorption, shorter transmission distances also benefit from a substantially larger channel bandwidth, which again contributes to the increase of achievable data-rates. However, the need for more hops to cover the same distance and the computational cost of relaying data at multi-Gbps or even Tbps poses major constraints on the system design. In addition, the impact of distance on the required DA gains and, consequently, beamwidths, again affect the system performance through the aforementioned MAC and neighbor discovery implications. Moreover, the queuing delay needs to be taken into account, particularly since we are dealing with very fast transmission speeds. The queuing delay plays a key role in the total end-to-end (E2E) delay, and is likely to increase when more relays are involved in the communication link.

In this paper, we study new cross-layer relaying strategies for multi-hop communications in the THz band. More specifically, first, we derive a mathematical framework to smartly allocate the resources across layers by optimizing the distribution of relays and ultimately achieve the smallest E2E delay. The developed framework takes into account the effects from not only the physics of the hardware and the channel, e.g., transmission power, DA beamwidth, transmission distance and operating bandwidth in the case of line of sight propagation, but also the MAC layer protocol design, e.g., interference and re-transmission, and the queuing delay when transmitting at multi-Gbps rates with buffer/memory limitations. The framework is based on a quasi-birth-death (QBD) Markov process model, which captures the capabilities and the behavior of a node in THz communication networks. This QBD model consists of a series of levels, including boundary level and repeating levels. The repeating levels stand for the number of packets currently queued in one specific node. The boundary level represents the status that the node does not have any packet to transmit. Within one repeating level, the transitions between different states are related to the re-transmission attempts that the packet will undergo. The transitions between inter-levels are further related to the queuing and dequeue probabilities and also the transmission(TX)/reception(RX) mode switching probabilities. We formulate the QBD Markov process model with all aforementioned cross-layer effects and, by utilizing the framework, we derive the distribution of relays to achieve the smallest E2E delay and the highest E2E throughput in different scenarios.

The remainder of this paper is organized as follows. First, in Sec. II, we summarize the related work and highlight the contribution of our work. Then, in Sec. III, we briefly describe the network topology and the nodes operation based on the receiver-initiated MAC protocol [17]. We also derive the peculiar distance-dependent feature of THz channel and the DA models. After this, in Sec. IV, we describe the overview of the QBD Markov process model for THz-band communication networks. Next, in Sec. V, we construct the QBD Markov process model with the intra-level states, which are defined based on the receiver-initiated MAC protocol. We also take into account the physical channel effects in the states transition design. Then, in Sec. VI, we mathematically derive the inter-level transitions of the QBD Markov process model. We model the enqueue and dequeue processes, as well as TX/RX mode switching processes. We also provide the solution of the QBD Markov process model. After this, in Sec. VII, we validate the analytical QBD Markov process model by means of MATLAB simulations and derive the performance analysis of E2E throughput for a multi-hop link. We conclude the paper in Sec. VIII.

II. RELATED WORK

Existing multi-hop relaying placement strategies developed for lower frequencies cannot be directly ported to THz-band communication networks, because they do not capture the aforementioned peculiarities of the THz channel. For instance, in [27], the authors chose the relays by optimally allocating the energy and bandwidth resources based on the available channel state information. This design is proposed for resource

This article has been accepted for publication in a future issue of this journal, but has not been fully edited. Content may change prior to final publication. Citation information: DOI 10.1109/TWC.2021.3136788, IEEE Transactions on Wireless Communications

constrained networks. In [28], the authors incorporated both user traffic demands and the physical channel realizations in a cross layer design to select the best relay. The approach is designed for a cellular system operating in a frequency-selective slow-fading environment.

To the best of our knowledge, there is no related work has been proposed for the macro-scale scenario in THz-band communication. Some works [29]–[31] studied on the similar relaying distribution problem by considering the physical channel conditions. However, they mainly focus on the nano-scale scenario in THz-band communication, which is different from our studied scenario in terms of bandwidth, antenna performance and MAC protocol.

Other than that, the mmWave technology (30 to 300 GHz) is the closest existing technology. Several similarities are shared between THz-band communication and mmWave-band communication. For instance, both technologies are designed for ultra-high data-rates communication and, similarly, both technologies suffer from very high path loss and, thus, require highly DAs to overcome this limitation. However, there are several differences between mmWave and THz-band communication networks, which arise from the fact that at THz frequencies, the absorption loss defines the THz band as a series of frequency-selective and distance-dependent frequency windows. The bandwidth shrinks with the increasing of transmission distance. However, for mmWave technology, the bandwidth is standardized and independent of the transmission distance. In addition, at THz frequencies, highly DAs are simultaneously needed in transmission and reception to complete any meaningful data transaction. However, at mmWave bands, a quasi-omni directional antenna together with a DA are usually utilized in transmission and reception.

In [32], the authors proposed a cross layer virtual time-slot allocation scheme for throughput enhancement in a mmWave multi-Gbps WPAN system, in which the cross layer design only considered the physical layer and MAC layer. In [33], [34], the authors improved the concurrent throughput for mmWave WPANs by applying hop section schemes, which is achieved by using scheduling schemes that explore the spatial reuse for concurrent transmission. However, due to very high path loss and low transmission power, spatial reuse is not feasible in THz-band communication networks. In [35], the authors introduced a cross-layer model to determine network link connectivity as a function of the location of relays. The approach took into accounts for two unique features of mmWave including interference and blockage, which can not be simply reused in THz-band communication network.

In [36], we proposed the first cross-layer design of THz-band communication networks, from physical layer to the design of data link layer and further to the multi-hop queuing system design in the network layer. However, this work is based on a simplified directive queuing model which does not consider the re-transmission limitation and the buffer capacity limitation of each node, nor the corresponding link-layer MAC protocol.

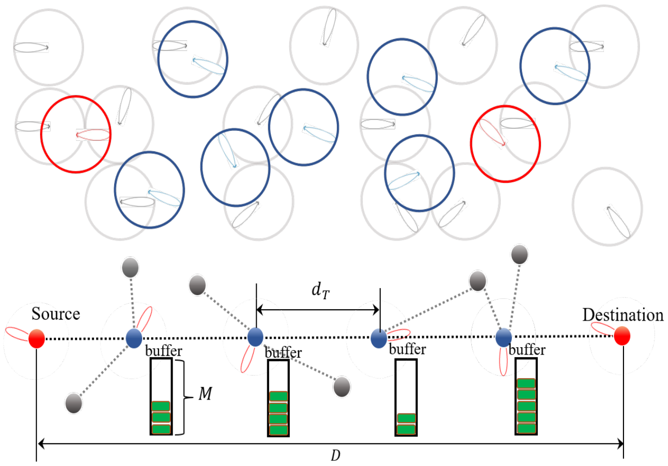

Fig. 1: Network architecture.

III. System Preliminaries

In this section, we first describe the scenario under analysis as well as the network topology and operation. Second, we introduce the THz-band channel model and present the energy consumption, THz-band channel frequency response and the molecular absorption noise power as functions of the transmission distance. Then, we introduce the DA model utilized in our analysis. We derive the DA characteristics, which include antenna gain and antenna beamwidth, as functions of the transmission distance. Finally, we describe the MAC protocols considered in our analysis.

A. Network Topology and Operation

We consider that all the nodes are randomly distributed in a flat area following a spatial Poisson distribution. Nodes operate using the receiver-initiated MAC protocol for directional THz networks proposed in [17], which was shown to outperform the more conventional transmitter-initiated MAC protocols in terms of throughput, drop probability and E2E. Accordingly, each node operates in half-duplex mode and periodically switches between transmission (TX) mode and reception (RX) mode. A node in TX mode, i.e., with data to transmit, checks whether a Clear-To-Send (CTS) frame from the intended receiver has been recently received, as we studied in [17]. We consider that a CTS frame is valid for the duration that transmitter and receiver within line of sight (LoS). The transmitter who has data to send to a specific receiver, can only proceed with the data transmission using a DATA frame after receiving a valid CTS frame from that receiver, otherwise, the transmitter listens to the channel until the reception of a new CTS frame. A node in RX mode periodically broadcasts its status with CTS frames.

We illustrate the network topology in Fig. 1. The network is formed as an ad-hoc architecture, whose coverage range can be extended with the help of the relays. Relays nodes, which help to relay other nodes' packets in addition to generating their own packets, are marked as blue nodes and are uniformly distributed in the whole network to guarantee network connectivity for any node in any direction. The remaining

This article has been accepted for publication in a future issue of this journal, but has not been fully edited. Content may change prior to final publication. Citation information: DOI 10.1109/TWC.2021.3136788, IEEE Transactions on Wireless Communications

TABLE I: Parameters and Constants

Symbol	Quantity
D	Distance between source-destination pair
d_T	Single hop transmission distance
P_r	Received signal power
S_t	Single-side power spectral density of the transmitted signal
B	3dB bandwidth
f	Operation frequency
H_c	THz-band channel frequency response
c	Speed of light
k_{abs}	Molecular absorption coefficient
N_r	Molecular absorption noise power
S_{NB}	Background atmospheric noise power spectral density
S_{NI}	Self-induced noise power spectral density
SNR_{min}	Minimum SNR threshold
G_t and G_r	Gain of transmitter antenna and receiver antenna, respectively
G	Desired antenna gain by considering $G_t(d_T) = G_r(d_T) = G(d_T)$
Ω_A	Array solid beam angle of DAs
θ_h and ϕ_h	Half Power Beam Width of DAs in the elevation plane and azimuthal plane respectively
$\Delta\theta$	Beam width of the DAs
θ_{tx}^{start} and θ_{rx}^{start}	Initial angle of transmitter DA and receiver DA respectively
ω_{tx} and ω_{rx}	Turning speed of transmitter DA and receiver DA respectively

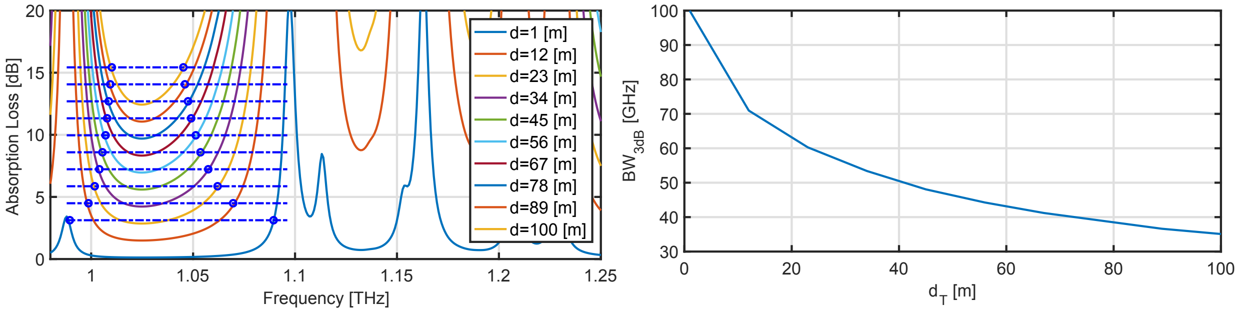

(a) Absorption loss defined window

(b) 3 dB bandwidth as a function of transmission range

Fig. 2: Absorption loss defined 3 dB bandwidth.

nodes, which never relay other nodes' packets, are marked as grey nodes. Within these, we have selected two as the source and the destination for the multi-hop E2E link analysis, colored in red. The goal of this paper is to determine the relay density and transmission range needed to achieve the maximum E2E throughput for such a network with multi-hop links. A summary of the parameters in our analysis is provided in Table I.

B. Channel Model

The unique distance-dependent characteristic of THz communication is caused by the physics of the channel. The propagation of electromagnetic waves at THz-band frequencies is mainly affected by molecular absorption, which is transmission distance dependent and frequency selective [10]. In this paper, we consider that nodes operate in the first absorption-defined window above 1 THz. The 3 dB window bandwidth varies with the transmission distance d_T, i.e., longer transmission distance results in a narrower 3 dB bandwidth window, see Fig. 2.

Molecular absorption results in both molecular absorption loss and molecular absorption noise, both of which, are transmission distance dependent parameters. In particular, the signal power at a transmission distance d_T from the transmitter is given by:

$$P_r(d_T) = \int_{B(d_T)} S_t(f) \left| H_c(f, d_T) \right|^2 G_t(d_T) G_r(d_T) \, df, \tag{1}$$

where S_t is the single-sided power spectral density (p.s.d) of the transmitted signal, B stands for the 3 dB bandwidth in respect of different transmission range. f refers to the operation frequency and H_c refers to the THz-band channel frequency response, which is given by [37]:

$$H_c(f, d_T) = \left(\frac{c}{4\pi f d_T} \right) e^{-\frac{k_{abs}(f) d_T}{2}}, \tag{2}$$

where c refers to the speed of light and k_{abs} is the molecular absorption coefficient of the medium, which is a frequency dependent value and is calculated based on the high-resolution transmission molecular absorption (HITRAN) database. The value of k_{abs} depends on the molecular composition of the transmission medium, i.e., the type and concentration of molecules found in the channel, and is computed as in [37]. G_t and G_r refer to the gain of transmitter antenna and receiver antenna, respectively, which in our study we consider that can be adapted according to the transmission distance (see next section).

Similarly, the molecular absorption noise power N_r at a distance d_T from the transmitter, can be modeled as additive, Gaussian, colored and correlated to the transmitted signal [38], and is given by:

$$N_r\left(d_T\right) = \int_{B(d_T)} \left(S_{N^B}\left(f\right) + S_{N^I}\left(f, d_T\right)\right) \left|H_r\left(f\right)\right|^2 df, \quad (3)$$

where it is taken into account that the total molecular absorption noise is contributed by the background atmospheric noise p.s.d., S_{N^B} and the self-induced noise p.s.d., S_{N^I}, and are computed as described in [38].

C. Directional Antenna Model

To overcome the very high molecular absorption loss over long distances and to increase the SNR, DAs are used at both the transmission and the reception with gains as G_t and G_r respectively. Such antennas can be realized either by means of directional antenna designs, such as horn antennas, or by utilizing beamforming antenna arrays [39].

The gains need to be calculated by taking into account the condition that the received signal strength should surpass the received signal power threshold, i.e.,

$$\int_{B(d_T)} S_t\left(f\right) \frac{c^2}{\left(4\pi d_T f\right)^2} e^{-k_{abs}(f) d_T} G_t\left(d_T\right) G_r\left(d_T\right) df \geq N_r\left(d_T\right) SNR_{min}, \quad (4)$$

where SNR_{min} stands for the minimum SNR threshold (10 dB in our analysis). Without loss of generality, the antenna gains of the transmitter and the receiver are considered to be identical and constant over the 3 dB frequency window, i.e., $G_t(d_T) = G_r(d_T) = G(d_T)$. In this case, the desired antenna gain can be expressed as:

$$G(d_T) \geq \sqrt{\frac{N_r\left(d_T\right) SNR_{min}}{\int_{B(d_T)} S_t\left(f\right) \frac{c^2}{\left(4\pi d_T f\right)^2} e^{-k_{abs}(f) d_T} df}}. \quad (5)$$

The directivity gain of highly DAs can be approximated as [40]:

$$G(d_T) \approx \frac{4\pi}{\Omega_A(d_T)} \approx \frac{4\pi}{\theta_h(d_T)\phi_h(d_T)}, \quad (6)$$

where Ω_A refers to the array solid beam angle, θ_h and ϕ_h are the Half Power Beam Width (HPBW) in the elevation plane and azimuthal plane, respectively. If we assume the HPBW in the elevation plane and azimuthal plane are identical, i.e., $\theta_h = \phi_h = \Delta\theta$, the beamwidth of the DA can be calculated as:

$$\Delta\theta(d_T) \leq \sqrt{4\pi \sqrt{\frac{\int_{B(d_T)} S_t\left(f\right) \frac{c^2}{\left(4\pi d_T f\right)^2} e^{-k_{abs}(f) d_T} df}{N_r\left(d_T\right) SNR_{min}}}}. \quad (7)$$

IV. OVERVIEW OF THE QUASI BIRTH DEATH MARKOV PROCESS

In this section, we provide an overview of the QBD Markov process for THz-band communication network model introduced in Sec. III. In a THz communication network, each node is represented by a queuing model, which accounts for the packet arrivals and departures as well as the service process of each packet. The QBD Markov process, as a generalization of the birth-death process, is utilized to comprehensively model the service behavior and analyze the distribution of the E2E delay of each packet. On the one hand, the QBD Markov process moves up and down between levels one at a time to capture the enqueue or dequeue behavior introduced by the cross layer nature of the network under analysis. On the other hand, the delay time of transitions between levels can have a more complicated distribution in the blocks of each level of the QBD Markov process. The block models the transmission/reception process of each packet taking into account the effects from the physics of the channel and the devices, namely, transmission power, communication distance, bandwidth and antenna beamwidth, or from the MAC layer protocol design, namely, interference and re-transmission.

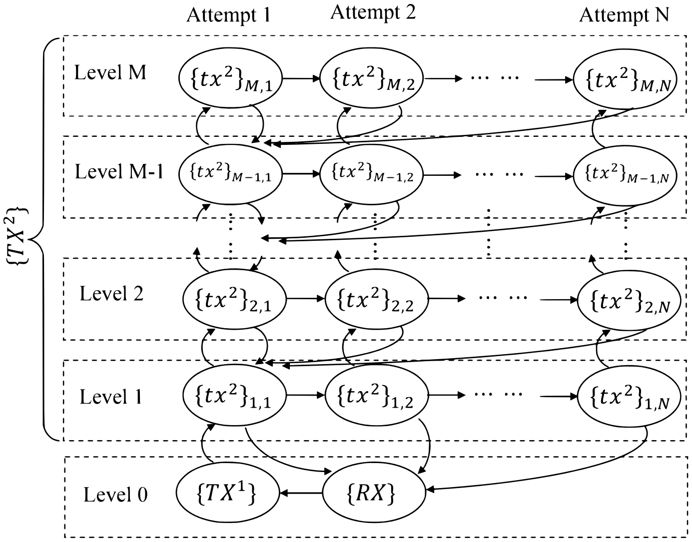

Fig. 3: QBD Markov process model of the system.

The QBD Markov process model shown in Fig. 3 consists of two types of levels, including boundary level and repeating levels. The repeating levels are the levels that satisfy the condition $1 \leq m \leq M$. We denote the maximum buffer capacity of each node as M. The index m represents the number of packets currently queued in node. The boundary level, satisfying $m = 0$, represents the status that the node does not have any packet to transmit. $\boldsymbol{\{RX\}}$ represents all states in RX mode. $\boldsymbol{\{TX^1\}}$ and $\boldsymbol{\{TX^2\}}$ are two components of the TX mode. $\boldsymbol{tx^2}$ is the basic component of $\boldsymbol{\{TX^2\}}$. More details are introduced in Sec. V.

Within one repeating level, the transitions between different states are related to the re-transmission attempts that the DATA packet will undergo. The number of the maximum DATA packet re-transmissions is defined in the MAC protocol and denoted as N. The transitions between inter-levels further relate to the queuing and dequeue probabilities and also the TX/RX mode switching probabilities. In all the transitions within a level and cross the levels, the cross-layer peculiarities of the THz-band communication networks are taken into account, including the channel, the antenna, the buffer and the physical, link and network layers. The detailed transitions

TABLE II: States Delay Duration

Notation	Parameter	Function
t_1^{rx}	Delay in "Send CTS"	$t_1^{rx} = T_{CTS} + T_{prop}$
t_2^{rx}	Delay in "CTS timeout"	$t_2^{rx} = N(T_{DATA} + T_{prop} + T_{ACK} + T_{prop})$
t_3^{rx}	Delay in "Receive DATA"	$t_3^{rx} = N(T_{DATA} + T_{prop}) + (N-1)(T_{ACK} + T_{prop})$
t_4^{rx}	Delay in "Send ACK"	$t_4^{rx} = T_{ACK} + T_{prop}$
t_0^{tx}	Delay in "Receive CTS"	$t_0^{tx} = T_{proc}^{CTS}$
t_1^{tx}	Delay in "Send DATA"	$t_1^{tx} = T_{DATA} + T_{prop}$
t_2^{tx}	Delay in "ACK timeout"	$t_2^{tx} = T_{ACK} + T_{prop}$
t_3^{tx}	Delay in "Send ACK"	$t_3^{tx} = T_{ACK} + T_{prop}$

$T_{CTS}, T_{DATA}, T_{ACK}$: Transmission delay of a CTS frame, DATA frame and ACK frame, respectively.
T_{prop}: Propagation delay.
T_{proc}^{CTS}: Processing delay of CTS frame.

within a level and cross levels are described in Sec. V and Sec. VI.

V. INTRA-LEVEL STATES AND TRANSITION MODEL BASED ON THZ MAC PROTOCOL

In this section, we describe the states within a level of the QBD Markov process. They are defined by the receiver-initiated MAC protocol described in Sec. III. Then, we incorporate the unique distance dependent properties, the directional THz communication feature and THz channel effects into the designed transitions between states inside one level.

A. *Overview of the Intra-level States in the QBD Process*

In Fig. 4, the intra-level states of the QBD process model, consisting of different element states, are shown. The duration of each state (summarized in Table II) differs from each other because of the different processing times associated to different packet types. The local DATA packet generation rate λ_l of each node is determined by the demands of the application layer. In this paper, we consider that λ_l follows a Poisson distribution and affects all states of the Markov process. Because of the half-duplex operation, a node cannot transmit and receive packets simultaneously. Thus, when nodes are in TX mode, the majority of TX duration is designed to send DATA packets. Even though there are time slots for receiving CTS and ACK frames during TX mode, these time slots are too short to accomplish a complete DATA packet reception. In this case, we consider that nodes cannot receive other nodes' DATA packets when they operate in TX mode. In contrast, nodes can help receive and relay other nodes' packets in most states of RX mode, except "Send CTS" and "Send ACK" states. Thus, only those blackened block-represented-states are affected by the relayed packets. The effects of packets arrival rate to the Markov process will be analyzed later in this section. A summary of the parameters in this section is shown in Table III.

The Markov process starts at "Send CTS" state in RX mode. After one sector duration T_{sector} of DA, the node switches from RX mode to TX mode. T_{sector} largely depends on N, which is the maximum number of DATA packet retransmission attempts during TX mode. When the buffer is full, the node starts to drop packets from the end of its buffer. A newly arrived DATA packet will push the buffer towards its capacity limitation, and the successful or the failed transmission of a DATA packet will release one DATA packet space from the buffer. Once there are no DATA packets left in the buffer, the node switches from TX mode to RX mode.

In Fig. 3, all states in RX mode are represented by $\{\boldsymbol{RX}\}$. TX mode consists of $\{\boldsymbol{TX^1}\}$ and $\{\boldsymbol{TX^2}\}$, which stand for the "Receive CTS" state and the DATA retransmission states, respectively. The basic component of $\{\boldsymbol{TX^2}\}$ is denoted as $\boldsymbol{tx^2}$, which represents the process of a DATA packet retransmission.

B. *$\boldsymbol{RX}$ Process*

We consider that the $\{\boldsymbol{RX}\}$ states and the $\{\boldsymbol{TX^1}\}$ states together construct the boundary level of the QBD Markov process model. For the purpose of simplification, we denote the combination boundary level as $\boldsymbol{RX}$ process. As shown in Fig. 4, the $\boldsymbol{RX}$ process consists of 5 states including "Send CTS," "CTS timeout," "receive DATA," "send ACK," and "Receive CTS," which are marked by an ascending order sequence from 1 to 5 for future notation. Based on the $\boldsymbol{RX}$ process illustrated in Fig. 4, the transition probability matrix is developed as:

$$\boldsymbol{P_{RX}(d_T)} = \begin{bmatrix} 0 & P_{1,2}^{rx}(d_T) & P_{1,3}^{rx}(d_T) & 0 & 0 \\ 0 & 0 & 0 & 0 & P_{rx}^{tx}(d_T)P_{0,1}^{tx}(d_T) \\ 0 & 0 & 0 & P_{3,4}^{rx} & 0 \\ 0 & 0 & 0 & 0 & P_{rx}^{tx}(d_T)P_{0,1}^{tx}(d_T) \\ 0 & 0 & 0 & 0 & 0 \end{bmatrix}, \quad (8)$$

where the format of $P_{i,j}^{rx}$ or $P_{i,j}^{tx}$ represents the probability that the $\boldsymbol{RX}$ process or the $\boldsymbol{tx^2}$ process changes from i^{th} state to j^{th} state, respectively. These probabilities are derived as follows:

- $P_{1,3}^{rx}$: is the probability that the node sends a CTS frame successfully and receives at least one DATA packet successfully within N maximum retransmission limitation, which is calculated as:

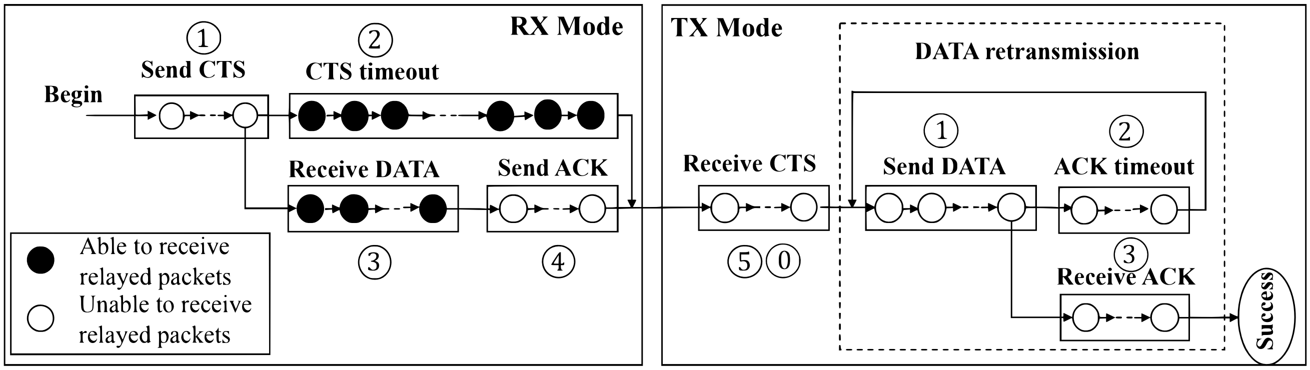

Fig. 4: MAC protocol.

TABLE III: Parameters and Constants of Intra-level Analysis

Symbol	Quantity
λ_l	Local DATA generation packet rate
R	Local DATA generation bit rate
λ_r	Relayed DATA packet generation rate
λ_g	Total DATA packet generation rate, $\lambda_g = \lambda_l + \lambda_r$
λ_n	Node density
T_{sector}	Sector duration of DA
N_{sector}	Number of sectors in one DA turning circle
N	Maximum number of DATA packet re-transmission attempts
M	Maximum buffer capacity of each node
$P^{rx}_{i,j}$ and $P^{tx}_{i,j}$	Probability that process change from i^{th} state to j^{th} state in RX mode and TX mode, respectively
$A^{x,y}_{coll}$	Interference area formed by the DA's coverage area
$n^{x,y}_I$	Expected nodes number within the interference area
$\boldsymbol{\pi}$	State probability vector
$\boldsymbol{P_{RX}}$	Transition probability matrix for the RX process
$\boldsymbol{\alpha_{RX}}$	Initial probability vector for RX process
$\boldsymbol{P^{suc}_{RX}}$ and $\boldsymbol{P^{fail}_{RX}}$	Probability vector for RX process to complete the transmission process successfully and unsuccessfully, respectively
$\boldsymbol{P_{tx^2}}$	Transition probability matrix of tx^2 process
$\boldsymbol{\alpha_{tx^2}}$	Initial probability vector for tx^2 process
$\boldsymbol{P^{suc}_{tx^2}}$ and $\boldsymbol{P^{fail}_{tx^2}}$	Probability vector for $\boldsymbol{tx^2}$ process to complete the transmission process successfully and unsuccessfully, respectively
$\boldsymbol{P_{\lambda_{tx^2}}}$	Packet arrival probability vector for tx^2 process
$\boldsymbol{P_{tx}}$	Transition probability matrix for a single repeating level
$\boldsymbol{\alpha_{tx}}$	Initial probability vector of a single level of Markov Queue
$\boldsymbol{P^{suc}_{tx}}$ and $\boldsymbol{P^{fail}_{tx}}$	Probability vectors to complete a single level of Markov Queue successfully and unsuccessfully respectively
$\boldsymbol{P_{\lambda_{tx}}}$	Packet arrival probability vector for single repeating level states

$$P^{rx}_{1,3}(d_T) = \overbrace{\left(1 - \prod_{y=1}^{n^{x,y}_I(d_T)} \left(1 - P^y_{S^{0,0}_{tx}}\right)\right)}^{\text{(9-a)}} \overbrace{\frac{1}{(N_{sector}(d_T))^2}}^{\text{(9-b)}} \overbrace{P^{suc}_{CTS}(d_T)}^{\text{(9-c)}} \overbrace{P\{n^{S_{cts}}_{DATA} \in T^{life}_{CTS}(d_T)\}}^{\text{(9-d)}} \underbrace{\left(1 - \left(1 - P^{suc}_{DATA}(d_T)\right)^N\right)}_{\text{(9-e)}}. \tag{9}$$

The component (9-a) is the probability that there is at least one transmitter node y currently able to establish one hop communication link with the node x, which is the receiver that just sent a CTS frame. To establish the link, y is currently in $S^{0,0}_{tx}$ state, which is the state of "Receive CTS". The probability that y is at state $S^{0,0}_{tx}$ is denoted as $P^y_{S^{0,0}_{tx}}$, which can be found in the state vector $\boldsymbol{\pi}$ of the Markov chain. $n^{x,y}_I$ represents the expected number of nodes in the interference area of one hop communication range and is calculated as:

$$n^{x,y}_I(d_T) = \sum_{i=1}^{\infty} i \frac{\left(\lambda_n A^{x,y}_{coll}(d_T)\right)^i}{i!} e^{-\lambda_n A^{x,y}_{coll}(d_T)}, \tag{10}$$

where λ_n is node density, $A^{x,y}_{coll}$ represents the interference area formed by the DA's coverage area of node x and node y, which can be calculated as:

$$A^{x,y}_{coll}(d_T) = 2d_T^2 \tan\left(\frac{\Delta\theta(d_T)}{2}\right). \tag{11}$$

The component (9-b) is the facing probability of node x and node y, where N_{sector} stands for the number of sectors in DA's complete turning circle, thus:

$$N_{sector}(d_T) = \frac{2\pi}{\Delta\theta(d_T)}. \tag{12}$$

This article has been accepted for publication in a future issue of this journal, but has not been fully edited. Content may change prior to final publication. Citation information: DOI 10.1109/TWC.2021.3136788, IEEE Transactions on Wireless Communications

The component (9-c) is the probability that node x sends CTS frame successfully, which is calculated as:

$$P^{suc}_{CTS}(d_T) = \left(1 - P^{coll}_{CTS}(d_T)\right)\left(1 - PER^{QPSK}_{CTS}(d_T)\right), \quad (13)$$

where PER^{QPSK}_{CTS} refers to the packet error rate of the CTS frame by using QPSK, which can be derived based on [41]. P^{coll}_{CTS} refers to the collision probability of sending a CTS frame, which is calculated as:

$$P^{coll}_{CTS}(d_T) = \left(1 - \overbrace{P\{0 \in A^{x,y}_{coll}(d_T)\}}^{\text{(14-a)}}\right)\left(1 - \overbrace{P\{0 \in 2FT_{CTS}(d_T)\}}^{\text{(14-b)}}\right). \quad (14)$$

The component (14-a) represents the probability that no node is located in the DAs' interference area of node x and node y, thus:

$$P\{0 \in A^{x,y}_{coll}(d_T)\} = e^{-\lambda_n A^{x,y}_{coll}(d_T)}. \quad (15)$$

The component (14-b) represents the probability that there is no DATA packet generated during the CTS frame vulnerable time, which is calculated as:

$$P\{0 \in 2FT_{CTS}(d_T)\} = e^{-\lambda_g(d_T)2FT_{CTS}(d_T)}, \quad (16)$$

where λ_g is the total DATA packet generation rate consists of the local DATA packet generation rate λ_l and the relayed DATA packet generation rate λ_r. FT_{CTS} is the transmission time of a CTS frame .

The component (9-d) represents the probability that node y generates $n^{S_{cts}}_{DATA}$ DATA packets towards node x during the CTS life time, given that $T^{life}_{CTS} = T_{sector}$, thus:

$$\begin{aligned} P\{n^{S_{cts}}_{DATA} \in T^{life}_{CTS}(d_T)\} &= P\{n^{S_{cts}}_{DATA} \in T_{sector}(d_T)\} \\ &= \sum_{n^{S_{cts}}_{DATA}=0}^{\infty} \frac{\left(\frac{\lambda_l T_{sector}(d_T)}{N_{sector}(d_T)}\right)^{n^{S_{cts}}_{DATA}}}{n^{S_{cts}}_{DATA}!} e^{-\frac{\lambda_l T_{sector}(d_T)}{N_{sector}(d_T)}}, \end{aligned} \quad (17)$$

where the DATA packet generation rate that towards the direction of node x is calculated as λ_l/N_{sector}.

The component (9-e) is the probability that at least one DATA packet is successfully received with N maximum retransmission limitation. P^{suc}_{DATA} is the probability that a DATA packet has been successfully transmitted and received, thus:

$$P^{suc}_{DATA}(d_T) = \left(1 - P^{coll}_{DATA}(d_T)\right)\left(1 - PER^{QPSK}_{DATA}(d_T)\right), \quad (18)$$

where P^{coll}_{DATA} and PER^{QPSK}_{DATA} refer to the collision probability and the packet error rate of DATA packets, respectively, which are calculated by using the same methodology as we applied in (13).

- $P^{rx}_{1,2}$: refers to the probability of CTS timeout caused by the failure of either CTS or DATA transmission, thus:

$$P^{rx}_{1,2}(d_T) = 1 - P^{rx}_{1,3}(d_T). \quad (19)$$

- $P^{rx}_{3,4}$: is the probability that after receiving DATA packet, the node replies an ACK frame. Since it is a strict rule of the MAC protocol, we have:

$$P^{rx}_{3,4} = 1. \quad (20)$$

- P^{tx}_{rx}: stands for the probability that node x transfers from RX mode to TX mode, which can be calculated as:

$$P^{tx}_{rx} = P^{rx}_{1,2}(d_T) + P^{rx}_{1,3}(d_T)P^{rx}_{3,4} = 1. \quad (21)$$

- $P^{tx}_{0,1}$: represents the probability of the node, now performs as a transmitter, received a CTS frame from a receiver node successfully and generates at least one DATA packet to the receiver node during the CTS frame life time. Since the node under study switches from RX mode to TX mode, we mark it as y, and the receiver node as x, thus:

$$\begin{aligned} P^{tx}_{0,1}(d_T) = &\overbrace{\left(1 - \prod_{x=1}^{n^{x,y}_I(d_T)} \left(1 - P^x_{S^{1,1}_{rx}}\right)\right)}^{\text{(22-a)}} \frac{1}{(N_{sector}(d_T))^2} \\ &P^{suc}_{CTS} P\{n^{S_{cts}}_{DATA} \in T^{life}_{CTS}(d_T)\}, \end{aligned} \quad (22)$$

where the component (22-a) is the probability that at least one node x, that able to establish one hop communication link with node y, and is currently in the states of "send CTS", which is the 1^{st} state, $S^{1,1}_{rx}$, in the RX mode. $P^x_{S^{1,1}_{rx}}$ is the probability of the receiver node in states $S^{1,1}_{rx}$, which is indicated in the state probability vector $\boldsymbol{\pi}$ of the Markov chain.

We consider that the initial probability vector of $\boldsymbol{RX}$ process is $\boldsymbol{\alpha_{RX}} = \begin{bmatrix}1, & 0, & 0, & 0, & 0\end{bmatrix}^T$, the probability vector for $\boldsymbol{RX}$ process to complete the transmission process successfully/unsuccessfully are $\boldsymbol{P^{suc}_{RX}} = \begin{bmatrix}0, & 0, & 0, & 1, & 1\end{bmatrix}$ and $\boldsymbol{P^{fail}_{RX}} = \begin{bmatrix}0, & 1, & 0, & 0, & 1\end{bmatrix}$, respectively.

C. $\boldsymbol{tx^2}$ Process

As shown in Fig. 3, the states in $\{\boldsymbol{tx^2}\}$ construct the repeating levels of the QBD Markov process model, which we denote as $\boldsymbol{tx^2}$ process. The $\boldsymbol{tx^2}$ process represents a complete retransmission process, which consists of "Send DATA, ACK timeout" and "Receive ACK" states and marked by an ascending order sequence from 1 to 3 as shown in Fig. 4. In light of the communication process illustrated in Fig. 4, the transition probability matrix of $\boldsymbol{tx^2}$ process is:

$$\boldsymbol{P_{tx^2}(d_T)} = \begin{bmatrix} 0 & P^{tx}_{1,2}(d_T) & P^{tx}_{1,3}(d_T) \\ 0 & 0 & 0 \\ 0 & 0 & 0 \end{bmatrix}, \text{ where} \quad (23)$$

- $P^{tx}_{1,3}$ is the probability that node y successfully send one DATA packet and receive an ACK frame.

$$P^{tx}_{1,3}(d_T) = P^{suc}_{DATA}(d_T)P^{suc}_{ACK}(d_T) \quad (24)$$

- $P^{tx}_{1,2}$ stands for the probability that node y failed to send DATA or to receive ACK frame.

$$P^{tx}_{1,2}(d_T) = 1 - P^{tx}_{1,3}(d_T). \quad (25)$$

We consider the initial probability vector of $\boldsymbol{tx^2}$ process is $\boldsymbol{\alpha_{tx^2}} = \begin{bmatrix}0, & 0, & 0\end{bmatrix}^T$, the probability vector for $\boldsymbol{tx^2}$ process to complete the transmission process successfully/unsuccessfully are $\boldsymbol{P^{suc}_{tx^2}} = \begin{bmatrix}0, & 0, & 1\end{bmatrix}$ and $\boldsymbol{P^{fail}_{tx^2}} = \begin{bmatrix}0, & 1, & 0\end{bmatrix}$, respectively. For the reason that the packet arrival probability vector for each state in $\boldsymbol{tx^2}$ process affects the buffer occupancy rate

This article has been accepted for publication in a future issue of this journal, but has not been fully edited. Content may change prior to final publication. Citation information: DOI 10.1109/TWC.2021.3136788, IEEE Transactions on Wireless Communications

and, thus, the performance of the Markov process. The packet arrival probability vector can be calculated as:

$$\boldsymbol{P}_{\lambda_{tx^2}}(\boldsymbol{d_T}) = \left[P_{\lambda_g}^{tx_1^2}(d_T),\ P_{\lambda_g}^{tx_2^2}(d_T),\ P_{\lambda_g}^{tx_3^2}(d_T)\right], \tag{26}$$

where the format $P_{\lambda_g}^{tx_k^2}$ is the probability that at least one DATA packet arrives the transmitter node y at the k^{th} state in $\boldsymbol{tx^2}$ process, giving that the DATA packets arrival rate is λ_g, thus:

$$P_{\lambda_g}^{tx_k^2}(d_T) = 1 - P\{0 \in t_k^{tx}(d_T)\} = 1 - e^{-\lambda_g(d_T)t_k^{tx}(d_T)}, \tag{27}$$

where t_k^{tx} is the duration of the k^{th} state of the Markov process, which is described in Table II.

D. Construction of Single Repeating Level of the QBD Markov Process

In Fig. 3, each repeating level consists of N retransmission processes $\boldsymbol{tx^2}$. Each retransmission process is triggered by the failure of previous DATA packet transmission. Thus, the transition probability matrix for a single repeating level of the QBD Markov process is calculated as:

$$\boldsymbol{P_{tx}}(\boldsymbol{d_T}) = \begin{bmatrix} \boldsymbol{P_{tx^2}}(\boldsymbol{d_T}) & \alpha_{\boldsymbol{tx^2}}\boldsymbol{P_{tx^2}^{fail}} & \cdots & \boldsymbol{0} & \boldsymbol{0} \\ \boldsymbol{0} & \boldsymbol{P_{tx^2}}(\boldsymbol{d_T}) & \cdots & \boldsymbol{0} & \boldsymbol{0} \\ \vdots & \vdots & \ddots & \vdots & \vdots \\ \boldsymbol{0} & \boldsymbol{0} & \cdots & \boldsymbol{P_{tx^2}}(\boldsymbol{d_T}) & \alpha_{\boldsymbol{tx^2}}\boldsymbol{P_{tx^2}^{fail}} \\ \boldsymbol{0} & \boldsymbol{0} & \cdots & \boldsymbol{0} & \boldsymbol{P_{tx^2}}(\boldsymbol{d_T}) \end{bmatrix}. \tag{28}$$

We further develop the initial probability vector of a single repeating level as $\boldsymbol{\alpha_{tx}} = \left[\alpha_{\boldsymbol{tx^2}},\ \boldsymbol{0},\ \cdots,\ \boldsymbol{0}\right]^T$, the probability vectors to complete a single repeating level successfully/unsuccessfully are $\boldsymbol{P_{tx}^{suc}} = \left[\boldsymbol{P_{tx^2}^{suc}},\ \boldsymbol{P_{tx^2}^{suc}},\ \cdots,\ \boldsymbol{P_{tx^2}^{suc}}\right]$ and $\boldsymbol{P_{tx}^{fail}} = \left[\boldsymbol{P_{tx^2}^{fail}},\ \boldsymbol{P_{tx^2}^{fail}},\ \cdots,\ \boldsymbol{P_{tx^2}^{fail}}\right]$, respectively. Considering that once the system is in the n^{th} retransmission state ($1 < n \leq N$), the previously failed DATA packets must be retransmitted, regardless if there is any new arrived DATA packet in the queue. The possibility of having a packet ready to transmit is one. The packet arrival probability vector for single repeating level states is thus developed as $\boldsymbol{P}_{\lambda_{tx}}(\boldsymbol{d_T}) = \left[\boldsymbol{P}_{\lambda_{tx^2}}(\boldsymbol{d_T}),\ \boldsymbol{1},\ \cdots,\ \boldsymbol{1}\right]$.

VI. INTER-LEVEL ANALYSIS OF THE QBD MARKOV PROCESS

In this section, the inter-level transitions of the QBD Markov process model are further analyzed. First, we conduct the states transition analysis according to the enqueue and dequeue process as well as the TX/RX mode switching. Then, we provide the solution of the QBD Markov process model. A summary of the parameters in our analysis is shown in Table IV.

A. States Transition with Buffer Capacity Limitation

To analyze the transition process between levels in the QBD Markov process model with buffer capacity limitation, we adopt the similar methodology introduced in [42]. For any level m, satisfying $1 \leq m \leq M-1$, the retransmission process transits to a higher level when a new packet arrives. The probability matrix of such transition is:

$$\boldsymbol{P_{tx}^{up}}(\boldsymbol{d_T}) = \left(\boldsymbol{1}\boldsymbol{P}_{\lambda_{tx}}(\boldsymbol{d_T})\right) \bigotimes \boldsymbol{P_{tx}}(\boldsymbol{d_T}), \tag{29}$$

where $\boldsymbol{1}$ is a properly dimensioned matrix containing all 1s, $\bigotimes$ is the Hadamard product. $\boldsymbol{P}_{\lambda_{tx}}$ and $\boldsymbol{P_{tx}}$, as defined in Sec. V-D, refer to the packet arrival probability vector and the transition probability matrix for a single repeating level, respectively.

When the node attempts to retransmit a DATA packet, the process stays at the same level m, with $1 \leq m \leq M-1$. The transition matrix of the retransmission process is calculated as:

$$\begin{aligned} \boldsymbol{P_{tx}^{same}}(\boldsymbol{d_T}) = {} & \overbrace{\left(\boldsymbol{1}\boldsymbol{P}_{\lambda_{tx}}(\boldsymbol{d_T})\right) \bigotimes \left(\alpha_{\boldsymbol{tx}}\left(\boldsymbol{P_{tx}^{suc}} + \boldsymbol{P_{tx}^{fail}}\right)\right)}^{\text{(30-a)}} + \\ & \overbrace{\left(\boldsymbol{1} - \boldsymbol{1}\boldsymbol{P}_{\lambda_{tx}}(\boldsymbol{d_T})\right) \bigotimes \boldsymbol{P_{tx}}(\boldsymbol{d_T})}^{\text{(30-b)}}, \end{aligned} \tag{30}$$

where the first component (30-a) represents the probability that a new DATA packet arrives to the buffer at the same time when the recently transmitted DATA packet is removed from the buffer because of either successful or failed transmission. The second component (30-b) represents the probability that there is no DATA packet arrives to or been removed from the buffer.

At the highest level $m = M$, the queue is full. Any newly arrived DATA packet or recently transmitted DATA packet that meets the retransmission limitation is directly dropped, accordingly, we have:

$$\boldsymbol{P_{tx}^{drop}}(\boldsymbol{d_T}) = \boldsymbol{P_{tx}^{up}}(\boldsymbol{d_T}) + \alpha_{\boldsymbol{tx}}\left(\boldsymbol{P_{tx}^{suc}} + \boldsymbol{P_{tx}^{fail}}\right). \tag{31}$$

For any level m, with $1 \leq m \leq M$. When no DATA packet arrives and the current DATA packet service is completed, the transmission process transits to a lower level. The transition matrix of this process is:

$$\boldsymbol{P_{tx}^{down}}(\boldsymbol{d_T}) = \left(\boldsymbol{1} - \boldsymbol{1}\boldsymbol{P}_{\lambda_{tx}}(\boldsymbol{d_T})\right) \bigotimes \left(\alpha_{\boldsymbol{tx}}\left(\boldsymbol{P_{tx}^{suc}} + \boldsymbol{P_{tx}^{fail}}\right)\right). \tag{32}$$

To complete the entire QBD Markov process, we extend our analysis to interrelate the boundary level with the repeating levels as follows. We consider that when a new DATA packet arrives, if RX mode time has not expired, the arrival of the new DATA packets will not affect the operation of RX mode. When RX mode time has expired, i.e., the system has experienced a complete process of RX mode, the Markov process transmits from $\boldsymbol{RX}$ process to $\boldsymbol{tx^2}$ process, and thus:

$$\boldsymbol{P_{rx}^{up}}(\boldsymbol{d_T}) = \left(\boldsymbol{P_{RX}^{suc}} + \boldsymbol{P_{RX}^{fail}}\right)^T \alpha_{\boldsymbol{tx}}^T. \tag{33}$$

TABLE IV: Parameters and Constants of Inter-level Analysis

Symbol	Quantity
$\boldsymbol{P_{tx}^{up}}$	Probability of the transition matrix of the retransmission process goes to the upper level
$\boldsymbol{P_{tx}^{same}}$	Probability of the transition matrix of the retransmission process stays at the same level
$\boldsymbol{P_{tx}^{drop}}$	Probability of the transition matrix of the retransmission process drops packets at the highest level
$\boldsymbol{P_{tx}^{down}}$	Probability of the transition matrix of the retransmission process goes to the lower level
$\boldsymbol{P_{rx}^{up}}$	Probability that the Markov process transmits from RX process to TX^2 process
$\boldsymbol{P_{rx}^{same}}$	Probability of the transition matrix stays at the RX level
$\boldsymbol{P_{rx}^{down}}$	Probability that the Markov process transmits from TX^2 to RX process

When the node in $\boldsymbol{tx^2}$ process completes the last DATA packet transmission, the buffer is empty, the Markov process transmits from $\boldsymbol{tx^2}$ to $\boldsymbol{RX}$ process, thus, we have:

$$\boldsymbol{P_{rx}^{down}} = \left(\boldsymbol{P_{tx}^{suc}} + \boldsymbol{P_{tx}^{fail}}\right)^T \alpha_{\boldsymbol{RX}}^T. \tag{34}$$

If there is no arriving DATA packet, the transition process stay in $\boldsymbol{RX}$ level, thus:

$$\boldsymbol{P_{rx}^{same}(d_T) = P_{RX}(d_T)}. \tag{35}$$

With the above analysis, we develop our entire QBD Markov process model for the cross-layer system as $\boldsymbol{P_{sys}}$, shown in (36).

B. Solution of Quasi-Birth-Death Markov Model

In this paper, we only consider the case with maximum buffer capacity $M \gg 2$. Based on this consideration, we summarize the conditions to calculate the rate matrix $\boldsymbol{R}$ and present them as follows:

$$\begin{cases} \boldsymbol{\pi_{m-1}(d_T)P_{tx}^{up}(d_T) + \pi_m(d_T)P_{tx}^{same}(d_T) + \pi_{m+1}P_{tx}^{down}(d_T)} \\ \boldsymbol{= \pi_m(d_T)} \\ \boldsymbol{\pi_m(d_T) = \pi_{m-1}(d_T)R(d_T)} \end{cases} \tag{37}$$

Thus, the rate matrix $\boldsymbol{R}$ is calculated as:

$$\begin{aligned} \boldsymbol{R(d_T)_{(n)}} = &- \left(\boldsymbol{P_{tx}^{up}(d_T) + R(d_T)_{(n-1)}^2 P_{tx}^{down}(d_T)}\right) \\ &\left(\boldsymbol{P_{tx}^{same}(d_T) - I}\right)^{-1}. \end{aligned} \tag{38}$$

We derive $\boldsymbol{R}$ iteratively by successive substitution making use of $\boldsymbol{R_{(1)} = 0}$. The iteration is repeated until two consecutive iterates satisfy $\left\|\boldsymbol{R_{(n+1)} - R_{(n)}}\right\| < \epsilon$, where ϵ is the predefined tolerance and $\|\cdot\|$ is an appropriate matrix norm.

By solving $\boldsymbol{\pi P_{sys} = \pi}$ and $\boldsymbol{\pi 1} = \sum_i \pi_i = 1$, we derive the equations as:

$$\begin{cases} \boldsymbol{\pi_0(d_T)P_{rx}^{same}(d_T) + \pi_1(d_T)P_{rx}^{down} = \pi_0(d_T)} \\ \boldsymbol{\pi_0(d_T)P_{rx}^{up}(d_T) + \pi_1(d_T)P_{tx}^{same}(d_T) + \pi_2 P_{tx}^{down}(d_T)} \\ \boldsymbol{= \pi_1(d_T)} \\ \boldsymbol{\pi_0(d_T)1 + \pi_1(d_T)(I - R(d_T))^{-1}1} = 1 \\ \boldsymbol{\pi_{M-1}(d_T)P_{tx}^{up}(d_T) + \pi_M(d_T)P_{tx}^{drop}(d_T) = \pi_M(d_T)} \end{cases}, \tag{39}$$

which can be rearranged as (40).

Therefore, we can calculate $\boldsymbol{\pi_0}$ and $\boldsymbol{\pi_1}$. Moreover, we solve $\boldsymbol{\pi_m}$ according to the second condition in (37), given that $2 \le m \le M-1$. For the highest level M, we calculate $\boldsymbol{\pi_M}$ based on the last condition of (39). In light of the above illustrations, the entire probability vector of the QBD Markov process model for our cross-layer system can be derived and denoted as:

$$\boldsymbol{\pi(d_T) = [\pi_0(d_T),\ \pi_1(d_T),\ \cdots,\ \pi_M(d_T)]}. \tag{41}$$

The steady state probability vector is achieved by updating the queueing system with the latest result until the difference between the latest consecutive results is negligible.

VII. PERFORMANCE AND ANALYSIS

In this section, first, we validate the analytical QBD Markov process model described in the previous sections by means of simulation. Then, we use this model to analyze the E2E performance of THz communication networks.

A. Validation of the QBD Markov process Model

We use MATLAB to simulate a multi-hop THz communication network which is composed of THz nodes. Unless otherwise stated, we define the network with the following system parameters: the THz nodes are randomly distributed in an interference area following a Poisson distribution and with node density λ_n as 1 node per m^2. The distance D between the source node and the destination node is 100 m, the interference area is calculated as $\pi\left(\frac{D}{2}\right)^2$. The local DATA packet generation rate λ_l is $\frac{R}{L_{DATA}}$ Packets per Second (PPS), where the DATA generation rate R is 100 Gbps. The maximum number of DATA packet re-transmissions N is set to 3, the maximum buffer capacity M of each node is set to 50 packets. The central frequency f_c is 1.03 THz, the transmission power P_t is 0 dBm, while the background noise N_r equals -90 dBm [9], [16]. QPSK is used at the physical layer. The control frame length is 17 bytes and the DATA packet length is 2,000 bytes.

To validate the QBD Markov process model described in sections IV, V and VI, we compare the normalized histogram of each state's probability evolution over time in the simulation, with the entire probability vector of the QBD Markov process model in (41), which is obtained from the proposed analytical model. We account only for the steady state of the network. Thus, the initial probabilities of all states at the beginning stage of the evolution are discarded. Besides, more than 200 evolution times are considered, which guarantees that the network achieved stability. The comparison results are shown in Fig. 5, from which, the simulation results and the numerical results from the steady state analysis of the QBD Markov process model match appropriately. From Fig. 5a, it clearly indicates that the most vulnerable buffer levels that

This article has been accepted for publication in a future issue of this journal, but has not been fully edited. Content may change prior to final publication. Citation information: DOI 10.1109/TWC.2021.3136788, IEEE Transactions on Wireless Communications

$$\boldsymbol{P_{sys}}(\boldsymbol{d_T}) = \begin{bmatrix} \boldsymbol{P_{rx}^{same}}(\boldsymbol{d_T}) & \boldsymbol{P_{rx}^{up}}(\boldsymbol{d_T}) & \boldsymbol{0} & \boldsymbol{0} & \cdots & \cdots & \boldsymbol{0} & \boldsymbol{0} \\ \boldsymbol{P_{rx}^{down}} & \boldsymbol{P_{tx}^{same}}(\boldsymbol{d_T}) & \boldsymbol{P_{tx}^{up}}(\boldsymbol{d_T}) & \boldsymbol{0} & \cdots & \cdots & \boldsymbol{0} & \boldsymbol{0} \\ \boldsymbol{0} & \boldsymbol{P_{tx}^{down}}(\boldsymbol{d_T}) & \boldsymbol{P_{tx}^{same}}(\boldsymbol{d_T}) & \boldsymbol{P_{tx}^{up}}(\boldsymbol{d_T}) & \cdots & \cdots & \boldsymbol{0} & \boldsymbol{0} \\ \boldsymbol{0} & \boldsymbol{0} & \boldsymbol{P_{tx}^{down}}(\boldsymbol{d_T}) & \boldsymbol{P_{tx}^{same}}(\boldsymbol{d_T}) & \cdots & \cdots & \boldsymbol{0} & \boldsymbol{0} \\ \boldsymbol{0} & \boldsymbol{0} & \boldsymbol{0} & \boldsymbol{P_{tx}^{down}}(\boldsymbol{d_T}) & \ddots & & \boldsymbol{0} & \boldsymbol{0} \\ \vdots & \vdots & \vdots & \vdots & & \ddots & \vdots & \vdots \\ \boldsymbol{0} & \boldsymbol{0} & \boldsymbol{0} & \boldsymbol{0} & \cdots & \cdots & \boldsymbol{P_{tx}^{same}}(\boldsymbol{d_T}) & \boldsymbol{P_{tx}^{up}}(\boldsymbol{d_T}) \\ \boldsymbol{0} & \boldsymbol{0} & \boldsymbol{0} & \boldsymbol{0} & \cdots & \cdots & \boldsymbol{P_{tx}^{down}}(\boldsymbol{d_T}) & \boldsymbol{P_{tx}^{drop}}(\boldsymbol{d_T}) \end{bmatrix} \tag{36}$$

$$\begin{aligned} &\left[\ \boldsymbol{\pi_0}(\boldsymbol{d_T}), \quad \boldsymbol{\pi_1}(\boldsymbol{d_T})\ \right] \begin{bmatrix} \boldsymbol{P_{rx}^{same}}(\boldsymbol{d_T}) - \boldsymbol{I} & \boldsymbol{P_{rx}^{up}}(\boldsymbol{d_T}) & \boldsymbol{1} \\ \boldsymbol{P_{rx}^{down}} & \boldsymbol{P_{tx}^{same}}(\boldsymbol{d_T}) - \boldsymbol{I} + \boldsymbol{R}(\boldsymbol{d_T})\boldsymbol{P_{tx}^{down}}(\boldsymbol{d_T}) & (\boldsymbol{I} - \boldsymbol{R}(\boldsymbol{d_T}))^{-1}\,\boldsymbol{1} \end{bmatrix} \\ &= \left[\ \boldsymbol{0}, \quad \boldsymbol{0}, \quad 1\ \right]. \end{aligned} \tag{40}$$

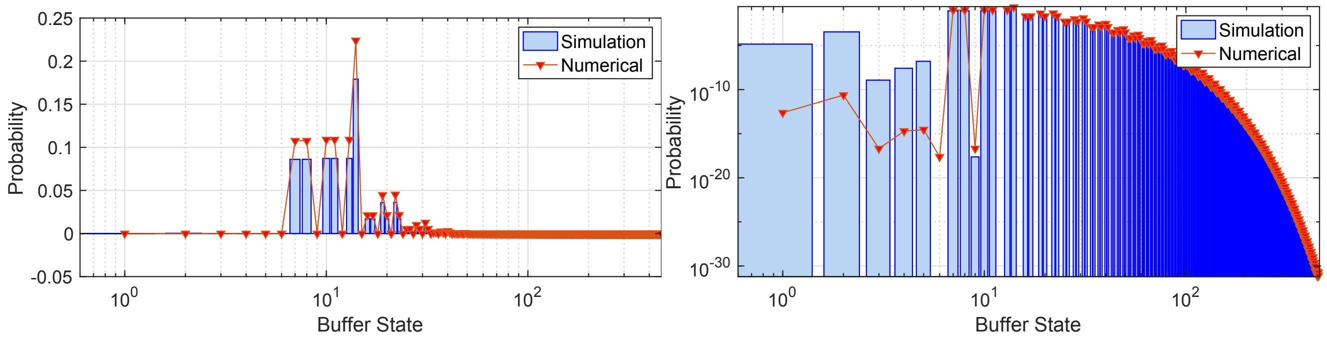

(a) Log-linear scale

(b) Log-log scale

Fig. 5: Entire probability vector of the QBD Markov process model in (41) (D = 100 m, R = 100 Gbps, M = 50 packets, $N = 3$).

suffer ongoing DATA packet re-transmissions are the lower buffer levels. In light of these results, next, we analyze the E2E performance of THz communication networks by means of the proposed QBD Markov process model.

B. Performance Metrics

The packet delay of the entire QBD Markov process of any single node is denoted as:

$$\boldsymbol{T_{delay}}(\boldsymbol{d_T}) = \left[\boldsymbol{T_0}(\boldsymbol{d_T}), \quad \boldsymbol{T_1}(\boldsymbol{d_T}), \quad \cdots, \quad \boldsymbol{T_M}(\boldsymbol{d_T})\right]^T, \tag{42}$$

where the format of $\boldsymbol{T_m}$ represents the delay duration in buffer level m, and is calculated by accumulating the duration that one DATA packet spent in all experienced states as partially indicated in Table II.

The single hop throughput is calculated as:

$$S_{hop}(d_T) = L_{DATA}/\left(\boldsymbol{\pi}(\boldsymbol{d_T})\boldsymbol{T_{delay}}(\boldsymbol{d_T})\right). \tag{43}$$

When multi-hop E2E communication link is considered to satisfy longer distance D between source-destination pair, the throughput of E2E communication link is calculated as:

$$S_{E2E}(d_T) = \frac{L_{DATA}}{\left(\boldsymbol{\pi}(\boldsymbol{d_T})\boldsymbol{T_{delay}}(\boldsymbol{d_T})\right) E_{hop}(d_T)}, \tag{44}$$

where $E_{hop}(d_T) = \lceil D/d_T \rceil$ is the expected hop number between source and destination.

C. Numerical Analysis

1) Throughput Analysis: As illustrated in Fig. 6a and 6b, we test the single hop throughput and the E2E multi-hop throughput for a fixed distance D between source and destination. The local packet generation rate R is set as an expected high rate to target the applications of THz communication, the buffer size of each node is 500 packets. As shown in Fig. 6a, the single hop throughput is a function of the maximum number of DATA packet re-transmission N. Small N effectively reduces the single level delay of the QBD Markov process model. Fig. 6a also suggests that the maximum single hop throughput occurs in the shortest transmission distance case. This is because transmitted packets suffer a huge propagation delay from operating under long transmission distance condition. However, as illustrated in Fig. 6b, the maximum throughput of the E2E multi-hop link shifts away from the shortest distance case. Since when nodes operate at longer transmission distance, reduced queueing delay for less hops compensates the longer propagation delay in single hop. The zigzag pattern of E2E multi-hop throughput is caused by the *ceil* function of E_{hop}. We curve-fit the E2E multi-hop throughput with the lower boundary to estimate the bottom line of the E2E throughput performance. For the parameters chosen in this section, the relaying distance to achieve the maximum E2E throughput is approximately 22 m, which would be well-

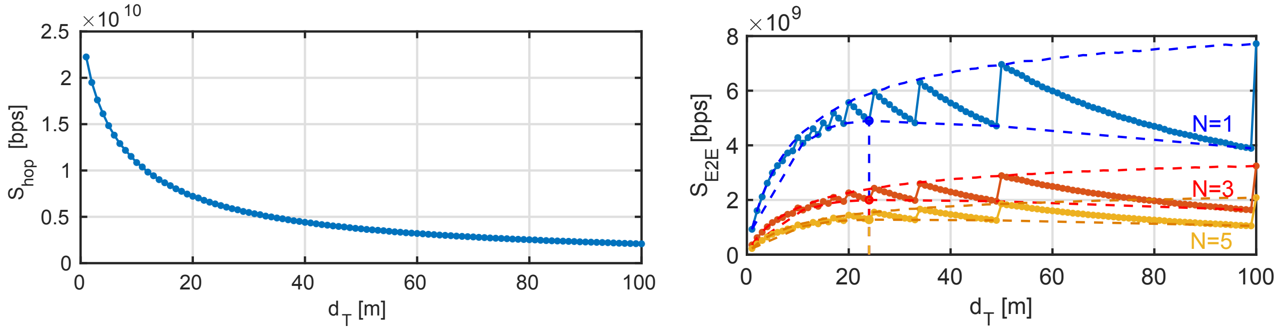

(a) Single hop throughput

(b) Throughput of E2E multi-hop link

Fig. 6: Single hop throughput v.s. throughput of E2E multi-hop link (D = 100 m, R = 100 Gbps, M = 500 packets).

aligned with backhaul-type applications [6].

2) Buffer Status Analysis: As illustrated in Fig. 7, we inspect the buffer status of each node. We check both the buffer occupancy rate of different groups of buffer levels, which is classified every 100 packets buffer levels, and the expected delay distribution of a DATA packets in the corresponding buffer groups. With an increasing single hop transmission distance d_T, longer propagation delay is triggered, which results in the growing of the expected packets delay in each buffer group. In Fig. 7a, we observe that without any DATA packet re-transmission ($N = 1$), the DATA packets only occupy the first buffer group, i.e., 0 packets $< m \leq$ 100 packets. While with more DATA packet re-transmissions allowed ($N = 3, 5$), as shown in Fig. 7b, 7c, more time is needed for a node to finish the complete process of DATA packet transmission/re-transmissions. Thus, with the same DATA packet generation rate R, DATA packets are gradually pushed up towards the higher buffer levels. However, the majority of the DATA packets still stored in the first buffer group.

3) Performance Analysis with Varying Packet Generation Rate: With an increasing local packet generation rate R, as shown in Fig. 8a, the maximum buffer occupancy rate grows almost at the same rate in all transmission distance cases. This is because, comparing with the removal rate of DATA packets, the packets arrival rate is not fast enough to drastically change the buffer occupancy rate distribution. Moreover, the probability vector of a DATA packet to achieve higher level states of our QBD Markov process model is too small to make a distinguished difference in the total delay. Thus, as indicated in Fig. 8b, with an increasing local packet generation rate, the throughput curve remains almost the same.

4) Performance Analysis with Varying Source-Destination Distance: As shown in Fig. 9a, the maximum buffer occupancy rate is affected by the distance D between source and destination pair. More specifically, longer D requires more relays, thus, tremendous relayed packets from more neighbor nodes push into the buffer much faster than the packet removal rate, and thus, leads to a higher buffer occupancy rate. As indicated in Fig. 9b, with the increasing D, the E2E throughput drops gradually because of both the longer delay in each relay and the increased queuing delay for more hops. The maximum throughput shifts to the longer transmission distance d_T side, which suggests to apply longer d_T to each relay.

5) Performance Analysis for long distance transmission: As shown in Fig. 10a, the distance D between the source and the destination is 1000 m. In the long communication distance case, since more hops are needed to establish the communication between the source and the destination, the buffer is easily saturated and the queuing delay increases. Thus, the throughput drastically drops compared with the short distance transmission cases. Also, longer single hop transmission distance d_T is always preferred to reduce the number of hops and to achieve higher E2E throughput. Other than that, the increased local packet generation rate does not change the throughput curve apparently, which is for the same reason as we analyzed in Fig. 8a. As a comparison, the throughput curve changes apparently with the variation of the distance D between the source and the destination, which is indicated in Fig. 10b. With the increasing D, the throughput drops gradually because of both the longer delay in each hop and the drastically increased queuing delay for more hops. The higher throughput is achievable with the longer single hop transmission distance d_T, which suggests to apply less number of hops between the source and the destination.

In the end, Table V summarized the effects on single hop throughput and the E2E throughput from independently increasing each key parameter of the studied scenario.

VIII. CONCLUSION

In this paper, we have explored the relaying strategies for THz-band communication networks. Based on the unique distance-dependent behavior of THz-band communication networks, a QBD Markov process model has been utilized and analyzed to derive the relaying distance to achieve the maximum E2E throughput, by taking into consideration the cross-layer effects between the channel, the highly directional antenna and the physical, link and network layers. The relaying performance with respect to several factors such as transmission distance, packets generation rate, buffer occupancy rate and the distance between source and destination have been numerically investigated. The extensive numerical results have been presented to demonstrate the importance of cross-layer design strategies for THz communication networks.

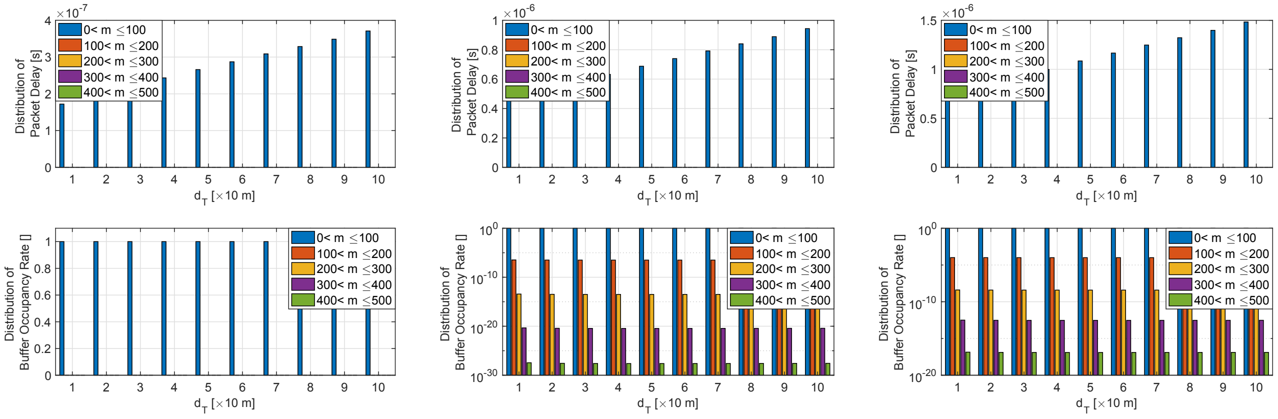

(a) $N = 1$ (b) $N = 3$ (c) $N = 5$

Fig. 7: Inspection of single node buffer status (D = 100 m, R = 100 Gbps, M = 500 packets).

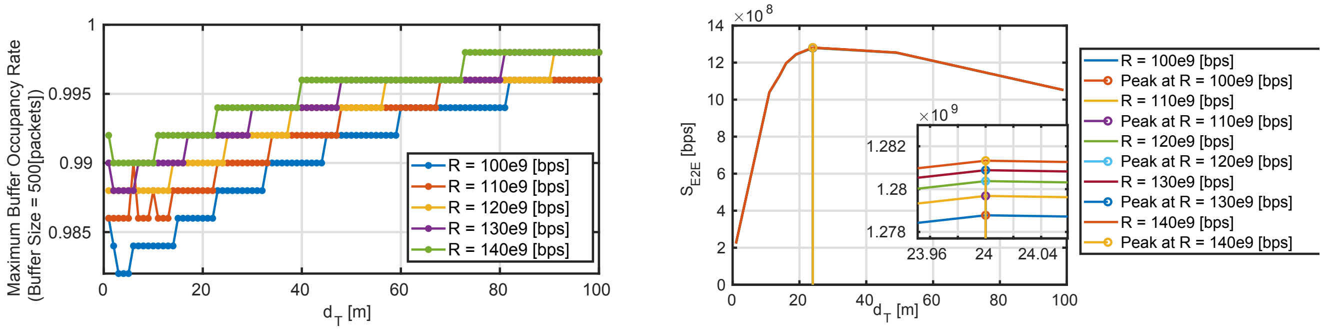

(a) Maximum buffer occupancy rate with varying R

(b) Throughput of E2E multi-hop link with varying R

Fig. 8: The maximum buffer occupancy rate and the throughput of E2E multi-hop link with varying R (D = 100 m, N = 5, M = 500 packets).

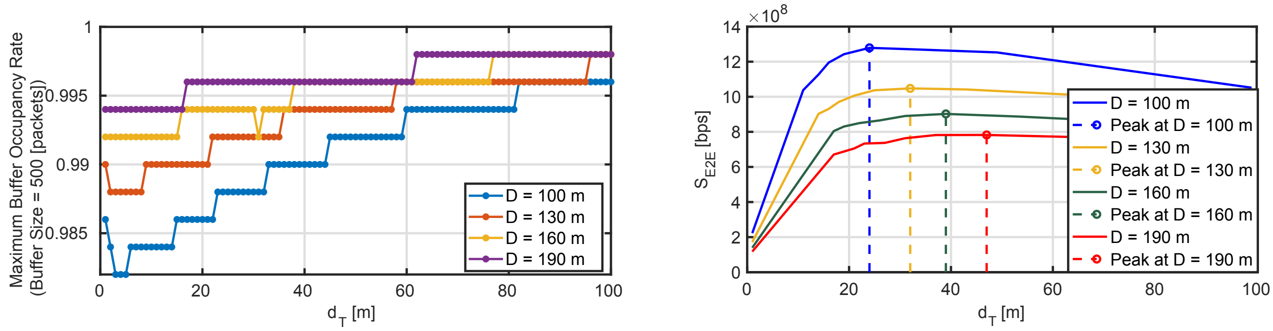

(a) Maximum buffer occupancy rate with varying D

(b) Throughput of E2E multi-hop link with varying D

Fig. 9: The maximum buffer occupancy rate and the throughput of E2E multi-hop link with varying D (R = 100 Gbps, N = 5, M = 500 packets).

REFERENCES

[1] Cisco annual internet report (2018–2023) white paper.

[2] I. F. Akyildiz, A. Kak, and S. Nie, "6g and beyond: The future of wireless communications systems," *IEEE Access*, vol. 8, pp. 133 995–134 030, 2020.

[3] *Samsung Electronics and University of California Santa Barbara Demonstrate 6G Terahertz Wireless Communication Prototype*, Jun 2021. [Online]. Available: https://news.samsung.com/global/samsung-electronics-and-university-of-california-santa-barbara-demonstrate-6g-terahertz-wireless-communication-prototype

[4] J. Federici and L. Moeller, "Review of terahertz and subterahertz wireless communications," *Journal of Applied Physics*, vol. 107, no. 11, p. 111101, 2010.

[5] H.-J. Song and T. Nagatsuma, "Present and future of terahertz communications," *IEEE Transactions on Terahertz Science and Technology*, vol. 1, no. 1, pp. 256–263, 2011.

[6] I. F. Akyildiz, J. M. Jornet, and C. Han, "Terahertz band: Next frontier

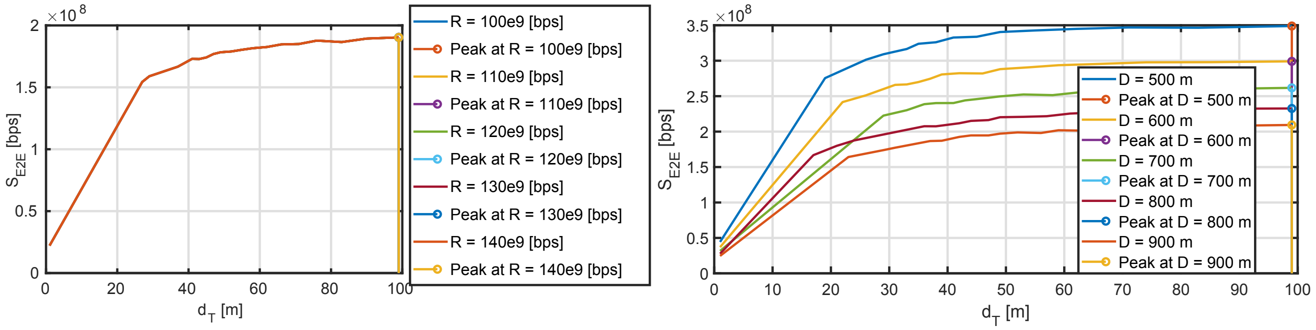

(a) Throughput of E2E multi-hop link with varying R

(b) Throughput of E2E multi-hop link with varying D

Fig. 10: The throughput of E2E multi-hop link with varying R ($D = 1000$ m, $N = 5, M = 500$ packets) and with varying D ($R = 100$ Gbps, $N = 5, M = 500$ packets).

TABLE V: Summary of Testing Parameters

Increasing Parameter	**Effect on single node throughput**	**Effect on E2E throughput**
Re-transmission Limitation (N)	Decreasing	Decreasing
Local DATA packet generation bit rate (R)	Slightly increasing (not fully buffered)	Slightly increasing (not fully buffered)
Single hop transmission distance ($d_T\,[m]$)	Decreasing	Optimal exist (first increase then decrease)
E2E distance ($D\,[m]$)	Decreasing	Decreasing

for wireless communications," *Physical Communication*, vol. 12, pp. 16–32, 2014.

[7] T. S. Rappaport, Y. Xing, O. Kanhere, S. Ju, A. Madanayake, S. Mandal, A. Alkhateeb, and G. C. Trichopoulos, "Wireless communications and applications above 100 ghz: Opportunities and challenges for 6g and beyond," *IEEE access*, vol. 7, pp. 78 729–78 757, 2019.

[8] K. Sengupta, T. Nagatsuma, and D. M. Mittleman, "Terahertz integrated electronic and hybrid electronic–photonic systems," *Nature Electronics*, vol. 1, no. 12, pp. 622–635, 2018.

[9] P. Sen, V. Ariyarathna, A. Madanayake, and J. M. Jornet, "Experimental wireless testbed for ultrabroadband terahertz networks," in *Proceedings of the 14th International Workshop on Wireless Network Testbeds, Experimental evaluation & Characterization*, 2020, pp. 48–55.

[10] J. M. Jornet and I. F. Akyildiz, "Channel modeling and capacity analysis for electromagnetic wireless nanonetworks in the terahertz band," *IEEE Transactions on Wireless Communications*, vol. 10, no. 10, pp. 3211–3221, October 2011.

[11] S. Priebe and T. Kurner, "Stochastic modeling of thz indoor radio channels," *IEEE Transactions on Wireless Communications*, vol. 12, no. 9, pp. 4445–4455, 2013.

[12] Y. Xing, T. S. Rappaport, and A. Ghosh, "Millimeter wave and sub-thz indoor radio propagation channel measurements, models, and comparisons in an office environment," *arXiv preprint arXiv:2103.00385*, 2021.

[13] Y. Chen, Y. Li, C. Han, Z. Yu, and G. Wang, "Channel measurement and ray-tracing-statistical hybrid modeling for low-terahertz indoor communications," *arXiv preprint arXiv:2101.12436*, 2021.

[14] C. Han, A. O. Bicen, and I. F. Akyildiz, "Multi-wideband waveform design for distance-adaptive wireless communications in the terahertz band," *IEEE Transactions on Signal Processing*, vol. 64, no. 4, pp. 910–922, 2015.

[15] Z. Hossain and J. M. Jornet, "Hierarchical bandwidth modulation for ultra-broadband terahertz communications," in *ICC 2019-2019 IEEE International Conference on Communications (ICC)*. IEEE, 2019, pp. 1–7.

[16] J. V. Siles, K. B. Cooper, C. Lee, R. H. Lin, G. Chattopadhyay, and I. Mehdi, "A new generation of room-temperature frequency-multiplied sources with up to 10× higher output power in the 160-ghz–1.6-thz range," *IEEE Transactions on Terahertz Science and Technology*, vol. 8, no. 6, pp. 596–604, 2018.

[17] Q. Xia, Z. Hossain, M. Medley, and J. M. Jornet, "A link-layer synchronization and medium access control protocol for terahertz-band communication networks," *IEEE Transactions on Mobile Computing*, vol. 20, no. 1, pp. 2–18, 2021.

[18] Z. Hossain, Q. Xia, and J. M. Jornet, "Terasim: An ns-3 extension to simulate terahertz-band communication networks," *Nano Communication Networks*, vol. 17, pp. 36–44, 2018.

[19] S. Ghafoor, N. Boujnah, M. H. Rehmani, and A. Davy, "Mac protocols for terahertz communication: A comprehensive survey," *IEEE Communications Surveys Tutorials*, vol. 22, no. 4, pp. 2236–2282, 2020.

[20] Q. Xia and J. M. Jornet, "Expedited neighbor discovery in directional terahertz communication networks enhanced by antenna side-lobe information," *IEEE Transactions on Vehicular Technology*, vol. 68, no. 8, pp. 7804–7814, 2019.

[21] T. Nitsche, A. B. Flores, E. W. Knightly, and J. Widmer, "Steering with eyes closed: Mm-wave beam steering without in-band measurement," in *2015 IEEE Conference on Computer Communications (INFOCOM)*, April 2015, pp. 2416–2424.

[22] F. Yildirim and H. Liu, "A cross-layer neighbor-discovery algorithm for directional 60-ghz networks," *IEEE Transactions on Vehicular Technology*, vol. 58, no. 8, pp. 4598–4604, Oct 2009.

[23] I. F. Akyildiz, C. Han, and S. Nie, "Combating the distance problem in the millimeter wave and terahertz frequency bands," *IEEE Communications Magazine*, vol. 56, no. 6, pp. 102–108, 2018.

[24] H. Sun, M. Naraghi-Pour, W. Sheng, and R. Zhang, "A hop-by-hop relay selection strategy in multi-hop cognitive relay networks," *IEEE Access*, vol. 8, pp. 21 117–21 126, 2020.

[25] A. Ikhlef, D. S. Michalopoulos, and R. Schober, "Max-max relay selection for relays with buffers," *IEEE Transactions on Wireless Communications*, vol. 11, no. 3, pp. 1124–1135, 2012.

[26] C. Chang, C. Chang, T. Wang, and M. Li, "Throughput-enhanced relay placement mechanism in wimax 802.16j multihop relay networks," *IEEE Systems Journal*, vol. 9, no. 3, pp. 728–742, 2015.

[27] Y. w. Hong, W. j. Huang, F. h. Chiu, and C. c. J. Kuo, "Cooperative communications in resource-constrained wireless networks," *IEEE Signal Processing Magazine*, vol. 24, no. 3, pp. 47–57, May 2007.

[28] T. C. y. Ng and W. Yu, "Joint optimization of relay strategies and resource allocations in cooperative cellular networks," *IEEE Journal on Selected Areas in Communications*, vol. 25, no. 2, pp. 328–339, February 2007.

[29] Q. H. Abbasi, A. A. Nasir, K. Yang, K. A. Qaraqe, and A. Alomainy, "Cooperative in-vivo nano-network communication at terahertz frequencies," *IEEE Access*, vol. 5, pp. 8642–8647, 2017.

[30] M. D. H. Zhichao Rong, Mark Stephen Leeson, "Relay-assisted nanoscale communication in the thz band," *Micro & Nano Letters*, vol. 12, pp. 373–376(3), June 2017.

[31] H. Yu, B. Ng, and W. K. G. Seah, "Forwarding schemes for em-based wireless nanosensor networks in the terahertz band," in *Proceedings of*

This article has been accepted for publication in a future issue of this journal, but has not been fully edited. Content may change prior to final publication. Citation information: DOI 10.1109/TWC.2021.3136788, IEEE Transactions on Wireless Communications

the Second Annual International Conference on Nanoscale Computing and Communication, ser. NANOCOM' 15. Association for Computing Machinery, 2015.

[32] C. S. Sum, Z. Lan, R. Funada, J. Wang, T. Baykas, M. A. Rahman, and H. Harada, "Virtual time-slot allocation scheme for throughput enhancement in a millimeter-wave multi-Gbps WPAN system," *IEEE Journal on Selected Areas in Communications*, vol. 27, no. 8, pp. 1379–1389, 2009.

[33] L. X. Cai, L. Cai, X. Shen, and J. W. Mark, "Rex: A randomized exclusive region based scheduling scheme for mmwave wpans with directional antenna," *IEEE Transactions on Wireless Communications*, vol. 9, no. 1, pp. 113–121, January 2010.

[34] J. Qiao, L. X. Cai, X. S. Shen, and J. W. Mark, "Enabling multi-hop concurrent transmissions in 60 ghz wireless personal area networks," *IEEE Transactions on Wireless Communications*, vol. 10, no. 11, pp. 3824–3833, November 2011.

[35] S. Singh, F. Ziliotto, U. Madhow, E. Belding, and M. Rodwell, "Blockage and directivity in 60 ghz wireless personal area networks: from cross-layer model to multihop mac design," *IEEE Journal on Selected Areas in Communications*, vol. 27, no. 8, pp. 1400–1413, October 2009.

[36] Q. Xia and J. M. Jornet, "Cross-layer analysis of optimal relaying strategies for terahertz-band communication networks," *in Proc. of the 13th IEEE international Conference on Wireless and Mobile Computing, Networking and Communications (WiMob)*, 2017.

[37] J. M. Jornet and I. F. Akyildiz, "Channel modeling and capacity analysis of electromagnetic wireless nanonetworks in the terahertz band," *IEEE Transactions on Wireless Communications*, vol. 10, no. 10, pp. 3211–3221, Oct. 2011.

[38] ——, "Femtosecond-long pulse-based modulation for terahertz band communication in nanonetworks," *IEEE Transactions on Communications*, vol. 62, no. 5, pp. 1742 – 1754, May 2014.

[39] A. Singh, M. Andrello, N. Thawdar, and J. M. Jornet, "Design and operation of a graphene-based plasmonic nano-antenna array for communication in the terahertz band," *IEEE Journal on Selected Areas in Communications*, vol. 38, no. 9, pp. 2104–2117, 2020.

[40] C. A. Balanis, *Antenna theory: analysis and design*. John Wiley & Sons, 2005.

[41] J. Proakis and M. Salehi, *Digital Communications*, ser. Asia Higher Education Engineering/Computer Science Electrical Engineering. McGraw-Hill, 2008. [Online]. Available: https://books.google.com/books?id=ksh0GgAACAAJ

[42] Y. Wang, M. C. Vuran, and S. Goddard, "Cross-layer analysis of the end-to-end delay distribution in wireless sensor networks," *IEEE/ACM Transactions on networking*, vol. 20, no. 1, pp. 305–318, 2012.

Qing Xia obtained her Ph.D. degree of Electrical Engineering from the University at Buffalo, The State University of New York. She was working as a Graduate Research Assistant under the guidance of Professor Josep Miquel Jornet at SUNY Buffalo. She received the B.S. degree in Electrical Engineering from Hebei University of Technology, Tianjin, China, and M.S. degree in Electrical Engineering from University of Denver, CO, USA, in 2010 and 2012, respectively. She was an intern with Intel Lab, OR, USA, in 2016. She is a member of the IEEE. She is currently working in Sony Corporation of America.

Dr. Josep M. Jornet (M'13, SM'20) received the B.S. in Telecommunication Engineering and the M.Sc. in Information and Communication Technologies from the Universitat Politècnica de Catalunya, Barcelona, Spain, in 2008. He received the Ph.D. degree in Electrical and Computer Engineering from the Georgia Institute of Technology (Georgia Tech), Atlanta, GA, in 2013. Between August 2013 and August 2019, he was a faculty with the Department of Electrical Engineering at the University at Buffalo (UB), The State University of New York. Since August 2019, he is an Associate Professor in the Department of Electrical and Computer Engineering, the Director of the Ultrabroadband Nanonetworking Laboratory, and a Member of the Institute for the Wireless Internet of Things at Northeastern University (NU), in Boston, MA. His research interests are in terahertz communication networks, wireless nano-bio-communication networks and the Internet of Nano-Things. In these areas, he has co-authored more than 180 peer-reviewed scientific publications, 1 book, and has also been granted 4 US patents. Since July 2016, he is the Editor-in-Chief of the Nano Communication Networks (Elsevier) Journal. He is serving as the lead PI on multiple grants from U.S. federal agencies including the National Science Foundation, the Air Force Office of Scientific Research and the Air Force Research Laboratory. He is a recipient of the National Science Foundation CAREER award and of several other awards from IEEE, ACM, UB and NU.